Strongly Coupled Pd Nanotetrahedron/Tungsten Oxide Nanosheet Hybrids with Enhanced Catalytic Activity and Stability as Oxygen Reduction Electrocatalysts

Yizhong Lu,[†,‡] Yuanyuan Jiang,[†,‡] Xiaohui Gao,[†,‡] Xiaodan Wang,[†] and Wei Chen*,[†]

[†]State Key Laboratory of Electroanalytical Chemistry, Changchun Institute of Applied Chemistry, Chinese Academy of Sciences, Changchun 130022, Jilin China

[‡]University of Chinese Academy of Sciences, Beijing 100039, China

S *Supporting Information*

ABSTRACT: The design and synthesis of highly active oxygen reduction reaction (ORR) catalysts with strong durability at low cost is extremely desirable but still remains a significant challenge. Here we develop an efficient strategy that utilizes organopalladium-(I) complexes containing palladium—palladium bonds as precursors for the synthesis of strongly coupled Pd tetrahedron—tungsten oxide nanosheet hybrids ($Pd/W_{18}O_{49}$) to improve the electrocatalytic activity and stability of Pd nanocrystals. The hybrid materials are synthesized by direct nucleation, growth, and anchoring of Pd tetrahedral nanocrystals on the in situ-synthesized $W_{18}O_{49}$ nanosheets. Compared to supportless Pd nanocrystals and

$W_{18}O_{49}$, their hybrids exhibited not only surprisingly high activity but also superior stability to Pt for the ORR in alkaline solutions. X-ray photoelectron spectroscopy, high-resolution transmission electron microscopy, and electrochemical analyses indicated that the enhanced electrocatalytic activity and durability are associated with the increased number and improved catalytic activity of active sites, which is induced by the strong interaction between the Pd tetrahedrons and $W_{18}O_{49}$ nanosheet supports. The present study provides a novel strategy for synthesizing hybrid catalysts with strong chemical attachment and electrical coupling between nanocatalysts and supports. The strategy is expected to open up exciting opportunities for developing a novel class of metal-support hybrid nanoelectrocatalysts with improved ORR activity and durability for both fuel cells and metal—air batteries.
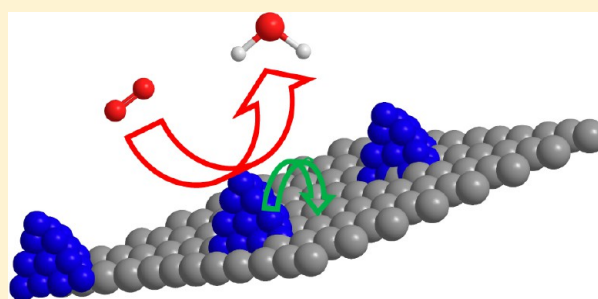
1. INTRODUCTION

Alkaline fuel cells (AFCs) and metal—air batteries offer an alternative solution to the low-temperature proton exchange membrane fuel cells (PEMFCs).[1,2] Compared to the acid environment of a PEMFC, an alkaline media provides a less corrosive environment to the catalysts and electrodes.[3] More importantly, in an AFC, the chemical energy in fuels can be directly and efficiently converted into electricity, which makes AFC a promising power supply for portable electronics. Unfortunately, the development of AFCs and metal—air batteries has been severely hampered by sluggish reaction kinetics of ORR, catalyst degradation and carbon-support corrosion.[4−7] So far, Pt- and Pt-based nanomaterials, particularly Pt black or Pt nanoparticles (2−5 nm) dispersed onto a carbon black support, has shown the highest ORR activity in alkaline media.[8,9] However, the practical large-scale commercialization of fuel cells is still a great challenge partially due to the high cost, limited supply, and declining activity of Pt-based catalysts during operation.[10] Therefore, the development of low-cost electrocatalysts with improved catalytic activity and durability is highly desirable but remains a significant challenge.[11−16]

As a potential replacement of Pt catalyst, palladium (Pd) has received considerable attention in comparison with other metal catalysts because of its relatively high ORR activity, stability, abundance, and low cost.[3,17−20] Actually, extensive studies have shown that Pd- and Pd-based nanomaterials exhibited ORR activity comparable to that of Pt/C in alkaline media.[21−26] In a recent study, Poon et al.[25] showed that amorphous Pd nanoparticles synthesized by electroless deposition on an electrode exhibited ORR catalytic activities and durability much higher than that of crystalline Pd nanoparticles and commercial Pt/C and Pd/C in KOH solution. Adzic and co-workers studied the ORR activities of different noble metals with a (111) facet in a 0.1 M NaOH solution and found that Pd(111) exhibited enhanced ORR activity which is very close to that of Pt(111).[27] A similar volcano-type of activity and surface electronic structure (the *d*-band center) relationship in acidic solution was also observed in alkaline media.[28−30] Of all the pure metals, Pt is the most active as it is located closest to the top of the volcano while Pd lies on the right declining side

with a little higher *d*-band center than Pt. For Pd-based catalysts, there is still room for improvement. On the other hand, earlier studies have shown that metals with a somewhat lower oxygen binding energy than Pt should have a higher rate of oxygen reduction.[31] Thus, in order to design Pd or Pd-based catalysts with better activities for ORR than Pt, a decrease of the Pd electron density (downshift of the d-band center) is needed. One promising alternative approach is to find proper supports that can promote the reactivity of Pd and Pd-based catalysts via strong electron coupling between Pd and support. More importantly, the compositional and structural complexity of such supported catalyst systems offers many degrees of freedom for tuning their catalytic properties. Recently, much interest has been focused on using robust metal oxide supports such as TaO_x, TiO_2, $Ti_{0.7}Mo_{0.3}O_2$, and WO_3, etc.[32−36] Definitely, the resulting catalyst/metal oxide hybrid nanomaterials exhibited improved activity and durability toward the ORR, owing to the synergetic effect between catalyst and the metal oxide support. Therefore, catalysts directly grown on support, which can efficiently maximize the support−catalyst contact and thus achieve the desired high catalytic activity and durability deserve to be systematically studied. Unfortunately, in situ growth of catalysts on supports currently lacks effective control over the desired size, morphology, and structure, and as a result, their catalytic potentials may not be fully realized.[37] Thus, rational design and synthesis of heterogeneous catalysts remains an unattained goal in catalysis research.

Here, for the first time, we develop an efficient strategy for the synthesis of strongly coupled Pd tetrahedron/tungsten oxide nanosheet hybrid nanomaterials ($Pd/W_{18}O_{49}$) by using organopalladium(I) complexes containing palladium−palladium bonds as precursors. The unique thin nanosheet structure of tungsten oxide offers a large surface area and stable anchoring sites for the in situ formation and subsequent attachment of Pd nanocrystals, which enables the full utilization of the catalyst surface by minimizing the agglomeration of Pd nanotetrahedrons and tungsten oxide nanosheets in turn. The electrochemical studies showed that, compared to the supportless Pd or $W_{18}O_{49}$ alone, their hybrids exhibited not only enhanced ORR electrocatalytic activity but also superior stability in alkaline media, which render them a class of high-performance catalyst for ORR. The unusually high catalytic activity could be attributed to the strong chemical interaction and electronic coupling effects between the Pd nanocrystals and $W_{18}O_{49}$ nanosheets, which can weaken the interaction between Pd and the nonreactive oxygenated species and thus provide more active sites for O_2 adsorption and activation. While the improved durability of the $Pd/W_{18}O_{49}$ hybrid nanomaterials could be attributed to the excellent mechanical stability, chemical stability, efficient electron pathway, and high conductivity provided by oxygen vacancies and/or defects generated during the synthesis[36] as well as the antiaggregation of Pd nanotetrahedron due to the strong coupling between Pd and $W_{18}O_{49}$ nanosheet support. The present study highlights a novel strategy for preparing high-performance hybrid nanocatalysts with strong coupling between catalyst and support and provides a new direction for catalyst performance optimization for next-generation fuel cells.

2. EXPERIMENTAL SECTION

Chemicals and Materials. Potassium tetrachloropalladate(II) (K_2PdCl_4, 98%, Aldrich), palladium(II) 2,4-pentanedionate (Pd-(acac)$_2$, Pd 34.7%, Alfa Aesar), tungsten hexacarbonyl (W(CO)$_6$, 99%, Acros), poly(vinylpyrrolidone) (PVP, K-30, Aldrich), hexadecyltrimethylammonium bromide (CTAB, 99.0%, Sigma), *N*,*N*-dimethylformamide (DMF, A.R., 99.5%,), acetone (A.R., Beijing Chemical Works), ethanol (A.R., Beijing Chemical Works), 2-propanol (A.R., Beijing Chemical Works), perfluorosulfonic acid−PTFE copolymer (Nafion, 5% w/w Solution, Alfa Aesar), potassium hydroxide (KOH, A.R., Tianjin Chemical Reagent Co. Ltd.), E-TEK Pt/C (nominally 20% by wt of 2−5 nm Pt nanoparticles on Vulcan XC-72R carbon support, Alfa Aesar). Pd/C (20%) was purchased from Alfa Aesar. Nanopure water with a resistivity of >18 MΩ cm was used in the present study. All chemicals were commercially available and used without further purification. Moreover, all glassware was washed with aqua regia (HCl/HNO$_3$ with a volume ratio of 3:1) and rinsed with ethanol and ultrapure water. (*Caution! Aqua regia is a very corrosive oxidizing agent, which should be handled with great care.*)

Synthesis of Strongly Coupled $Pd/W_{18}O_{49}$ Hybrid Nanomaterials. In a typical synthesis, K_2PdCl_4 (8 mg) and W(CO)$_6$ (50 mg) were mixed together with 10 mL of DMF and 2 ml anhydrous ethanol. After vigorous stirring for 15 min, the solution color changed from brown to light yellow. Then 50 mg of PVP and 50 mg of CTAB were added to the above mixture at room temperature and stirred for another 15 min. The resulting homogeneous mixture was transferred into a conventional oven and heated at 180 °C for 30 min before it was cooled to room temperature. The resulting colloidal products were collected by centrifugation and washed several times with an ethanol−acetone mixture. Finally, the obtained products were dissolved in 3 mL of ethanol for further use.

Synthesis of $[Pd_2(\mu\text{-}CO)_2Cl_4]^{2−}$ Intermediate via Pure CO. Typically, 8 mg of K_2PdCl_4 was dissolved in 10 mL of DMF solution. Then CO was introduced at ambient temperature under vigorous stirring. A color change from brown to light yellow was clearly seen during the first several minutes. After 15 min, the CO gas was removed and the $[Pd_2(\mu\text{-}CO)_2Cl_4]^{2−}$ intermediate was obtained.

Synthesis of Supportless Pd Nanoparticles. In a typical synthesis, 50 mg of PVP and 50 mg of CTAB were added to the above $[Pd_2(\mu\text{-}CO)_2Cl_4]^{2−}$ intermediate prepared via pure CO at room temperature and stirred for another 15 min. The resulting homogeneous mixture was transferred into a conventional oven and heated at 180 °C for 30 min before it was cooled to room temperature. The resulting colloidal products were collected by centrifugation and washed several times with an ethanol−acetone mixture. Finally, the obtained products were dissolved in 3 mL of ethanol for further use.

Material Characterization. Transmission electron microscopy (TEM) measurements were performed on a Hitachi H-600 operating at 100 kV. The samples were prepared by dropping an ethanol dispersion of samples onto carbon-coated copper TEM grids using pipettes and dried under ambient condition. High-resolution TEM (HRTEM) images and the corresponding live fast Fourier transform (FFT), high-angle annular dark-field scanning transmission electron microscopy (HAADF-STEM) images, element mapping, and EDX were all carried out on a JEM-2010 (HR) microscope operated at 200 kV. The composition of the products was determined by an inductively coupled plasma-atomic emission spectrometer (ICP-AES, X Series 2, Thermo Scientific USA). To determine the bulk composition of the hybrids and examine the crystallinity of the products, power X-ray diffraction (XRD) was performed on a D8 ADVANCE (Germany) using Cu Kα radiation with a Ni filter (λ = 0.154059 nm at 30 kV and 15 mA). The thickness of the tungsten oxide nanosheets was characterized by an atomic force microscopy (AFM) (Nanoscopt 8 Multimode Scanning Probe microscope (Vecco)) operating in contact mode with standard silicon nitride tips at room temperature under ambient conditions. For AFM measurements, the samples were drop-cast on freshly cleaved mica and dried at room temperature. X-ray photoelectron spectroscopy (XPS) measurements were performed by using a VG Thermo ESCALAB 250 spectrometer (VG Scientific) operated at 120 W. The binding energy was calibrated against the carbon 1s line. The specific surface area of the products was measured at 77.35 K on an automatic N_2 adsorption/desorption instrument (Quantachrome Instruments, version 3.01), and the samples were outgassed in vacuum at 200 °C for 24 h before
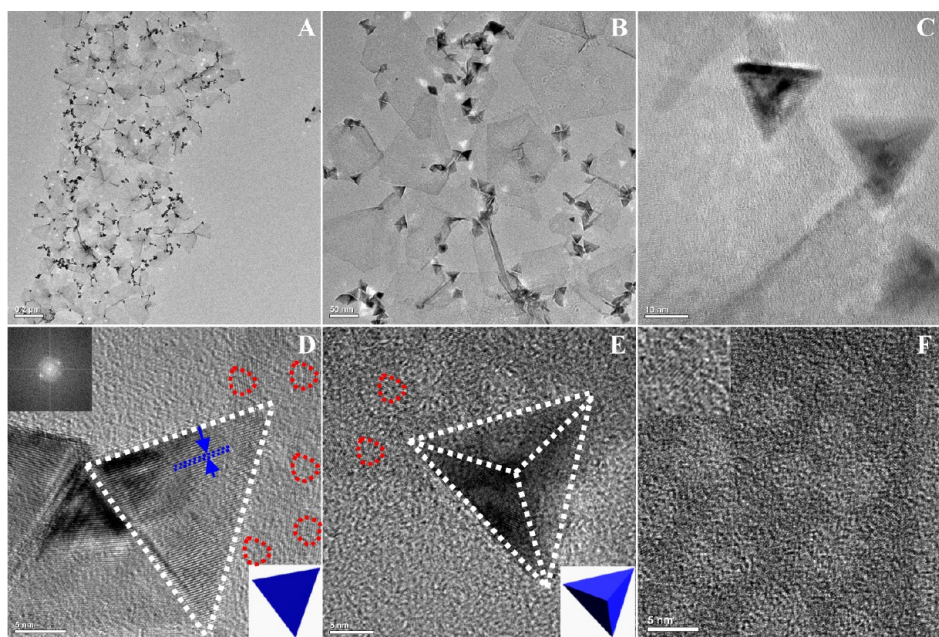
Figure 1. (A, B) Representative TEM images of the strongly coupled $Pd/W_{18}O_{49}$ hybrid nanomaterials (180 °C for 30 min) at different magnifications. (C−E) HRTEM images of the as-synthesized $Pd/W_{18}O_{49}$ at different orientations. The inset at the top left in D shows the FFT pattern of the Pd tetrahedron, and the insets at the bottom right in D and E are the corresponding crystal models, respectively. The inset in F shows the magnified HRTEM image of the $W_{18}O_{49}$ nanosheet.

testing. The specific surface area was calculated by the Brunauer−Emmett−Teller (BET) method using the adsorption branch in the relative pressure range from 0.05 to 0.30.

Electrochemical Measurements. All measurements were carried out with a CHI 750D electrochemical workstation in a standard three-electrode cell at room temperature. Working electrodes were prepared by mixing the catalyst with water, 2-propanol/ethanol and Nafion (5%) (v/v/v = 4/1/0.025) to form a 2 mg/mL suspension under sonication. A calculated amount of catalyst ink was deposited onto a RDE made of glassy carbon (geometric area 0.196 cm²), and the Pt or Pd loading of the thin-film catalysts on the RDE was adjusted to be 20 $\mu g/cm^2_{geo}$. A Pt coil and a saturated calomel electrode (SCE) combination isolated in a double junction chamber were used as the counter and reference electrode, respectively. All potentials referred to in this paper are converted to the pH-independent reversible hydrogen electrode (RHE), and the readout currents were recorded without any iR drop (ohmic drop caused by solution resistance) correction during the measurements. After being dried at room temperature under a gentle flow of nitrogen, the catalyst-coated glassy carbon working electrode was first wetted with nanopure water, attached to the shaft of the electrode rotator, and guided into the electrolyte. The working electrode should be positioned at the same height for each experiment to keep the solution resistance between the working electrode and SCE similar. Gas bubbles attached to the working electrode surface can be dislodged by rotation at higher speed. The gas flow rate is reduced during measurements to ensure that no additional bubbles stick to the working electrode surface. The potential was then continuously cycled between 0.2 and 1.1 V until a stable cyclic voltammogram was recorded (20 cycles at 100 mV/s). The minimum potential should be just above the potential for H₂ evolution, which will be scan rate and catalyst dependent. To avoid the corrosion of either the support or the catalyst itself, the positive limit of 1.1 V was never exceeded in any experiment.

The conductivities of the catalysts were evaluated by using cyclic voltammograms and electrochemical impedance spectroscopy (EIS) in N₂-saturated 5 mM $K_3Fe(CN)_6$ and 5 mM $K_4Fe(CN)_6$ mixture containing 0.1 M KCl. Cyclic voltammograms were conducted between −0.2 and 0.6 V (vs SCE) at a scan rate of 50 mV/s. The EIS was performed with the alternative current (AC) voltage amplitude of 5 mV, the voltage frequency ranging from 100 kHz to

0.05 Hz and the applied potential of 0.2 V (vs SCE). Linear-sweep voltammetry (LSV) measurements were conducted under an oxygen atmosphere by sweeping the potential from 1.1 V (vs RHE) cathodically to 0.2 V at a scan rate of 10 mV/s. The kinetic current (I_k) can be calculated using the Koutecky−Levich equation which is expressed by

$$I_k = I_d I/(I_d - I) \tag{1}$$

where I is the experimentally obtained current, I_d refers to the measured diffusion-limited current, and I_k is the mass-transport free kinetic current.

The I_d term can be obtained from the Levich equation:

$$I_d = 0.62nFAD^{2/3}v^{-1/6}\omega^{1/2}C_{O2} \tag{2}$$

where n is the number of electrons transferred, F is Faraday's constant (96 485 C/mol), A is the area of the electrode (0.196 cm²), D is the diffusion coefficient of O₂ in 0.1 M KOH solution (1.9×10^{-5} cm²/s), v is the kinematic viscosity of the electrolyte (0.01 cm²/s), ω is the angular frequency of rotation, $\omega = 2\pi f/60$, f is the RDE rotation rate in rpm, and C_{O2} is the concentration of molecular oxygen in 0.1 M KOH solution (1.2×10^{-3} mol/L).

Specific activities were determined via calculation of I_k and normalization with the electrochemically active surface area (ECSA) and the noble metal (Pt or Pd) loading. All experiments were repeated three times to confirm the reproducibility and to improve the accuracy in the determination of kinetic activities. The electrocatalytic activities of the catalysts toward ORR were quantified at $E = 0.90$ V because interferences from mass-transport losses cannot be completely excluded at higher current densities observed below 0.90 V. The accelerated durability tests (ADTs) of the catalysts were conducted by applying a cyclic potential sweep between 0.6 and 1.0 V (vs RHE) in O₂-saturated 0.1 M KOH solution at room temperature, with scan rate of 0.1 V/s and a rotation speed of 1600 rpm.

3. RESULTS AND DISCUSSION

Synthesis and Characterization of Pd Nanotetrahedrons Supported on Tungsten Oxide Nanosheets (Pd/$W_{18}O_{49}$). As described in Experimental Section, an efficient
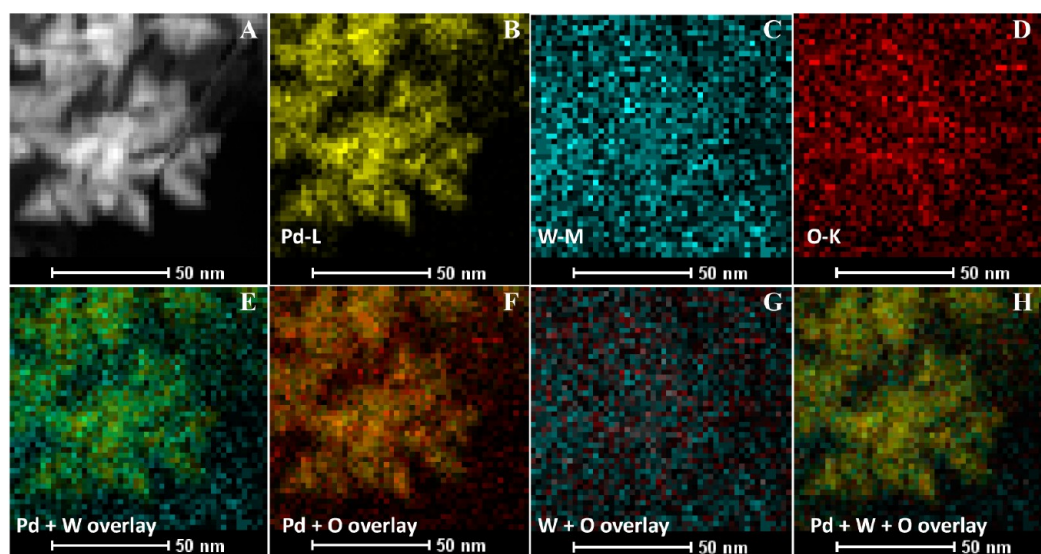
Figure 2. (A) The high-angle annular dark-field (HAADF)-STEM image of the $Pd/W_{18}O_{49}$ hybrids synthesized at 180 °C for 30 min, and the corresponding elemental mapping of (B) Pd, (C) W, (D) O, and the overlay of (E) Pd and W, (F) Pd and O, (G) W and O, and (H) Pd, W, and O.

one-pot strategy consisting of two steps was developed for the synthesis of strongly coupled Pd tetrahedron/tungsten oxide nanosheet ($Pd/W_{18}O_{49}$) hybrid nanomaterials. In the first step, a light yellow organopalladium(I) complex, $[Pd_2(\mu\text{-}CO)_2Cl_4]^{2-}$, which has been systematically characterized recently,[38] was first prepared under the assistance of $W(CO)_6$ at room temperature. In the second step, $W_{18}O_{49}$ nanosheet-supported Pd tetrahedrons were obtained through a hydro-thermal process with $[Pd_2(\mu\text{-}CO)_2Cl_4]^{2-}$ as the metal precursor. $W(CO)_6$ plays dual roles in the present strategy for the formation of $Pd/W_{18}O_{49}$ hybrid. First it can provide (CO) in the preparation of the organopalladium(I) complex and meanwhile $W_{18}O_{49}$ nanosheets can be in situ produced from $W(CO)_6$ during the formation of Pd nanotetrahedrons by hydrothermal treatment. The loading of Pd nanocrystals on the $W_{18}O_{49}$ nanosheets can be easily tuned by just changing the precursor ratio.

The typical TEM images of the as-prepared $Pd/W_{18}O_{49}$ hybrid (180 °C for 30 min) at different magnifications are illustrated in Figure 1A,B. Almost all the highly monodispersed Pd nanocrystals with a tetrahedral shape are uniformly dispersed on $W_{18}O_{49}$ nanosheets. An additional TEM image in Figure S1, Supporting Information, further demonstrates that Pd nanotetrahedrons could be obtained with >90% purity and in a relatively large quantity. It is interesting that in addition to the produced Pd tetrahedrons, very thin two-dimensional $W_{18}O_{49}$ nanosheets with sizes ranging from 80 to 500 nm also appear in Figure 1A,B. The morphology of the $Pd/W_{18}O_{49}$ hybrid was also characterized by high-resolution TEM. From the HRTEM images of individual nanocrystals shown in Figure 1C−E and Figure S2, Supporting Information, the as-synthesized Pd nanocrystals have regular tetrahedral shape with an average diameter of 19.67 nm. Each nanotetrahedron displays clear lattice fringes with interplanar spacing of 0.24 nm, corresponding to the (111) basal planes of the Pd tetrahedrons.[39] The corresponding fast Fourier-transform (FFT) pattern (Figure 1D inset) indicates the single crystal structure of the tetrahedral Pd nanoparticles. Surprisingly, the high-resolution TEM image of the $W_{18}O_{49}$ nanosheets (Figure 1F and the red cycles in Figure 1D,E) demonstrate that the

nanosheets have a two-dimensional (2D) network structure which may be formed from the fusion of a large number of small nanoparticles. The measured lattice distances of the $W_{18}O_{49}$ nanosheets corresponded to the monoclinic structure (JCPDS 36-101). Analogous results have recently also been reported for tungsten oxide nanoplates.[40] From the AFM image and the corresponding height cross-sectional profile shown in Figure S3, Supporting Information, the thickness of the $W_{18}O_{49}$ nanosheets was measured to be around 13 nm. By using the BET method, the specific surface area of the $W_{18}O_{49}$ nanosheet was determined to be 40.45 m^2/g, which is slightly larger than that of the nanosized tungsten oxide (29.9 m^2/g).[36] The large surface area of the $W_{18}O_{49}$ nanosheets can be ascribed to their unique 2D porous network structure. High angle annular dark-field scanning transmission electron microscopy (HAADF-STEM) images of the $Pd/W_{18}O_{49}$ and the corresponding elemental mapping (Figure 2) clearly demonstrate that the produced Pd tetrahedrons are well dispersed on $W_{18}O_{49}$ nanosheets.

The crystal structures of the as-synthesized materials were characterized by powder X-ray diffraction (XRD) analysis. As can be seen from Figure 3A, the diffraction pattern of the as-synthesized tungsten oxide matches well with the monoclinic-phase $W_{18}O_{49}$ ($WO_{2.72}$, JCPDS no. 36-101). In the XRD pattern of the $Pd/W_{18}O_{49}$, in addition to the signals from $W_{18}O_{49}$ nanosheets, the diffraction peaks centered at 40.25°, 46.33°, and 68.03° could be assigned to the (111), (200), and (220) crystal facets of metallic Pd with face-centered cubic crystalline structure (JCPDS no. 46-1043). The XRD results clearly indicate the successful synthesis of coupled $Pd/W_{18}O_{49}$ hybrid nanomaterials. The composition of the $Pd/W_{18}O_{49}$ hybrid nanomaterials were also confirmed by energy-dispersive X-ray (EDX) spectroscopy (Figure S4, Supporting Information) and inductively coupled plasma-atomic emission spectroscopy (ICP-AES). X-ray photoelectron spectroscopy (XPS) measurements were then performed to determine the chemical states and compositions of the as-synthesized $Pd/W_{18}O_{49}$ hybrids. The survey XPS of the hybrids (Figure 3B) clearly indicates the presence of Pd and W. As can be seen from the Pd XPS spectrum (Figure 3C), the peaks at 335.1 and 340.4 eV are
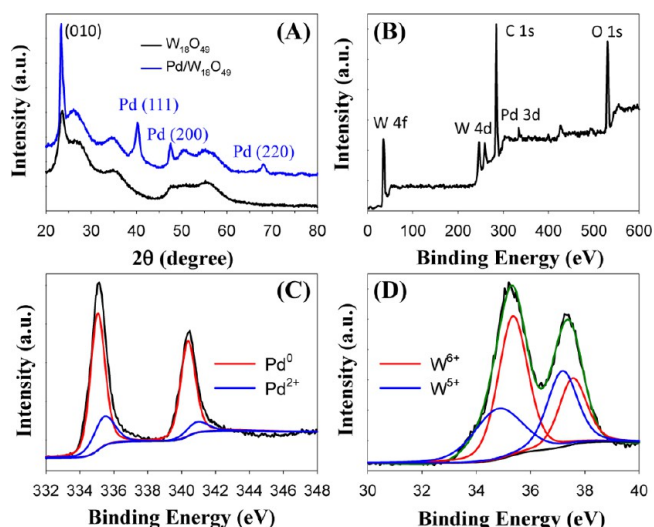
Figure 3. (A) XRD patterns of $W_{18}O_{49}$ nanosheets and the Pd/$W_{18}O_{49}$ hybrid nanomaterials. (B−D) XPS spectra of the strongly coupled Pd/$W_{18}O_{49}$ hybrid nanomaterials obtained at 180 °C for 30 min. (B) Survey spectrum; (C) Pd 3d and (D) W 4f.

attributed to the $3d_{5/2}$ and $3d_{3/2}$ binding energies of zerovalent state of metallic Pd, respectively. The binding energies at 335.7 and 341.0 eV correspond to the $3d_{5/2}$ and $3d_{3/2}$ levels of Pd^{2+} in the form of PdO on the surface of the Pd/$W_{18}O_{49}$ hybrids.[41,42] In Figure 3D, the W 4f doublet with the binding energies of 35.38 and 37.58 eV could be assigned to W^{6+} species,[36,43−45] while the W 4f doublet with binding energies of 34.88 and 37.16 eV corresponds to W^{5+}. Note that no elemental tungsten was observed in the present 2D $W_{18}O_{49}$ nanosheet support.[46,47] The O 1s patterns are displayed in Figure S5, Supporting Information, to further investigate the chemical states of oxygen in $W_{18}O_{49}$ and Pd/$W_{18}O_{49}$. The peak with binding energy at 530.2 eV corresponds to O 1s levels of oxygen atoms O^{2-} in the lattice of $W_{18}O_{49}$,[45] and the binding energy at 533.2 eV could be assigned to the adsorbed water molecules on the free oxide surface. Moreover, the peak at 531.8 may be due to the adsorbed CO molecules produced from the decomposition of $W(CO)_6$ and/or DMF. The XPS analyses indicate that the nanosheets are composed mainly of W^{5+} and W^{6+}.[48] The absorption spectra of the $W_{18}O_{49}$ nanosheets and Pd/$W_{18}O_{49}$ hybrids were compared in Figure 4A. It can be seen that in addition to the strong valence-to-conduction band transition absorption in the UV region, the formed thin $W_{18}O_{49}$ nanosheets also show a broad absorption

in the visible and NIR region, indicating the presence of oxygen vacancies in the $W_{18}O_{49}$ crystal structure. However, the Pd/$W_{18}O_{49}$ hybrids show low absorption in the visible and NIR region. The different absorption features suggest that there is strong coupling between the $W_{18}O_{49}$ nanosheets and Pd nanotetrahedrons, which can effectively enhance the electrocatalytic activity of the Pd/$W_{18}O_{49}$ hybrid. The strong coupling between Pd nanotetrahedrons and the $W_{18}O_{49}$ nanosheets is also demonstrated from the photoluminescence (PL) measurements. Figure 4B shows the PL spectra of $W_{18}O_{49}$ nanosheets and the Pd/$W_{18}O_{49}$. For the $W_{18}O_{49}$ nanosheets (red curve), a strong blue emission centered at ca. 425 nm can be observed, indicating the presence of large amount of oxygen vacancies.[44,49] The fluorescence features are similar to those observed from other 2D tungsten oxide thin films, which further suggests the 2D structure of the as-synthesized $W_{18}O_{49}$ nanosheets.[49−51] However, after the formation of Pd/$W_{18}O_{49}$ hybrids (black curve), the blue emission at 425 nm disappears, which further confirms that the oxygen vacancies on the surface of the $W_{18}O_{49}$ nanosheets could serve as active sites for the nucleation and growth of Pd nanocrystals.

To better understand the formation process of Pd/$W_{18}O_{49}$ hybrid, the evolution of the Pd nanocrystals at different reaction times was investigated by TEM. Figure 5 details the morphological evolution of the hybrids with reaction time. In the initial stage of the reaction (t = 1 min), well-defined Pd tetrahedrons with average size of 19.67 nm have been formed and homogeneously dispersed on a single $W_{18}O_{49}$ nanosheet, which indicates the fast reaction kinetics of the organopalladium(I) complex. With reaction time increasing, the Pd nanotetrahedrons retained their size and shape while nanosheets began to link together to form the 2D $W_{18}O_{49}$ nanosheets. After 30 min, no further morphology change of both Pd nanocrystals and $W_{18}O_{49}$ nanosheets can be observed.

To elucidate the experimental conditions and the mechanism of the formation of Pd/$W_{18}O_{49}$ hybrids, control experiments were performed. In the absence of $W(CO)_6$, only aggregates of Pd nanoparticles with irregular shapes were obtained under otherwise the same experimental conditions, as demonstrated in Figure S6A, Supporting Information. On the other hand, through reaction in the presence of $W(CO)_6$ but in the absence of K_2PdCl_4, 2D graphene-like $W_{18}O_{49}$ nanosheets were obtained as the final products (Figure S6B). Note that the reaction using $Pd(acac)_2$ instead of K_2PdCl_4 produced Pd polyhedral nanoparticles with an average size of about 16 nm (Figure S7, Supporting Information). More importantly, when the $[Pd_2(\mu\text{-}CO)_2Cl_4]^{2-}$ intermediate was prepared according to
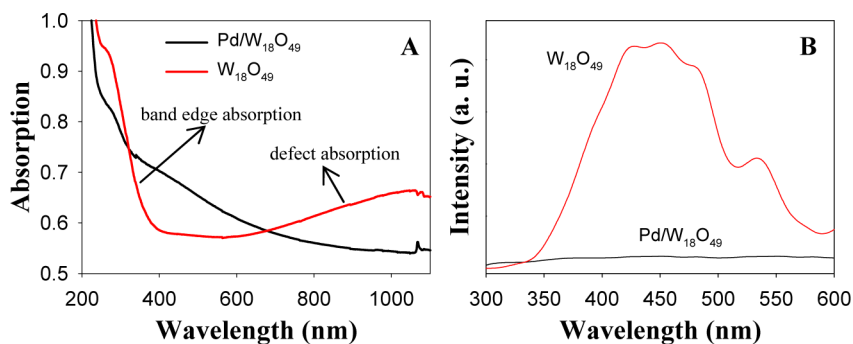

Figure 4. (A) UV−vis absorption and (B) photoluminescence spectra of the $W_{18}O_{49}$ nanosheets and the strongly coupled Pd/$W_{18}O_{49}$ hybrid nanomaterials.
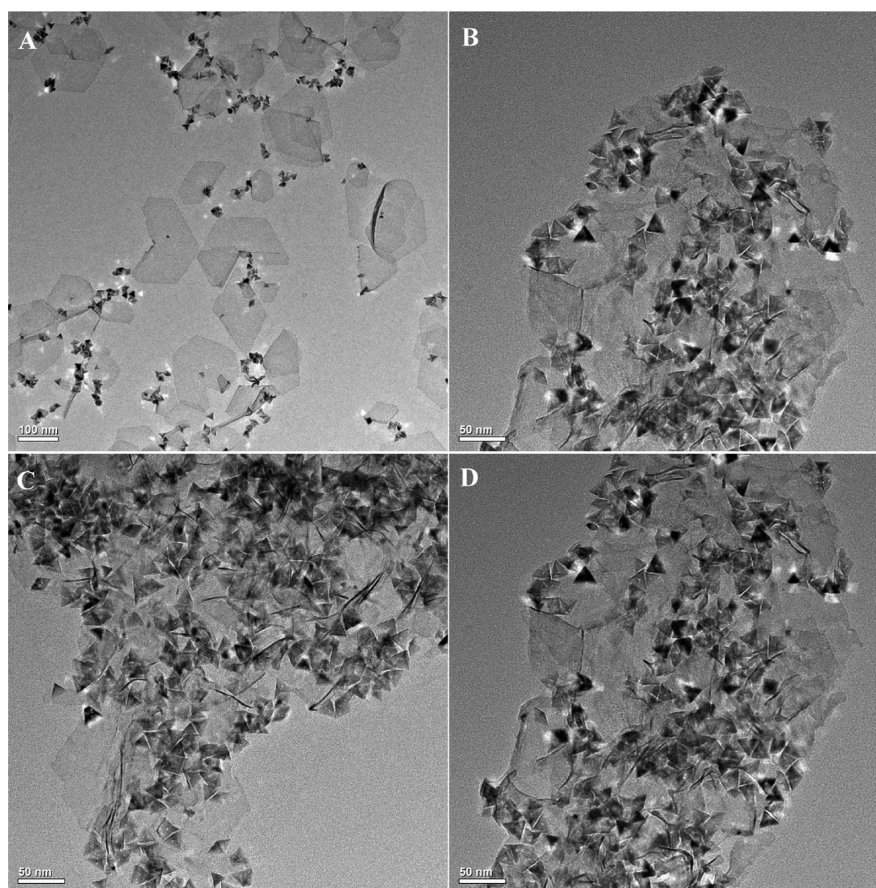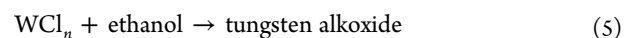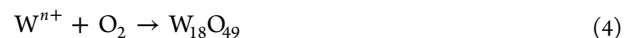
Figure 5. Representative TEM images of the $Pd/W_{18}O_{49}$ products collected at 180 °C for different reaction times: (A) 1 min, (B) 15 min, (C) 30 min, and (D) 60 min.

the earlier report by using CO^{38} instead of $W(CO)_6$, only supportless Pd nanoparticles with irregular shapes were obtained under similar reaction conditions (Figure S8, Supporting Information). On the basis of these results, it can be concluded that in our synthesis, the use of K_2PdCl_4 and $W(CO)_6$ is essential to the formation of Pd nanotetrahedron/ $W_{18}O_{49}$ nanosheet hybrids. In the previous report,[38] the intermediate, $[Pd_2(\mu\text{-}CO)_2Cl_4]^{2-}$, could be obtained from the reaction between $PdCl_4^{2-}$ and the CO molecule. Here we found that the reactive $[Pd_2(\mu\text{-}CO)_2Cl_4]^{2-}$ intermediate could be easily formed by mixing K_2PdCl_4 and $W(CO)_6$ in DMF solution, as can be seen from Scheme 1 and the color change (from brown to light yellow, Figure S9, Supporting Information). The color change is in good agreement with that reported previously.[38] Note that the as-synthesized $[Pd_2(\mu\text{-}CO)_2Cl_4]^{2-}$ is highly reactive, which can be reduced by simply mixing with water to form Pd nanosheets at room temperature (Figure S10, Supporting Information).

Compared to the $[Pd_2(\mu\text{-}CO)_2Cl_4]^{2-}$ prepared previously from CO, the present yellow intermediate formed from $W(CO)_6$ has a different structure. As shown in Scheme 1A, separated $[Pd_2(\mu\text{-}CO)_2Cl_4]^{2-}$ was formed from CO molecules. However, with $W(CO)_6$ as precursor, $W(CO)_x$-linked $[Pd_2(\mu\text{-}CO)_2Cl_4]^{2-}$ intermediate can be formed due to the strong covalent interaction between W and CO (Scheme 1B). On the other hand, the presence of $W(CO)_6$ could help reduce organopalladium(I) to Pd(0). For instance, we found that the yellow intermediates can be changed slowly to dark solution after aging for several days at room temperature (Figure S11,

Supporting Information). Under the hydrothermal condition, the reaction can be accelerated while, instead of the formation of ultrathin Pd nanosheets by H_2O reduction, tetrahedral Pd nanocrystals were produced and simultaneously supported on the W-containing nanosheets. Compared with the previously reported thermal decomposition of $W(CO)_6$,[47,52] we believe that the presence of O_2 in the present reaction system plays an important role for the formation of $W_{18}O_{49}$ nanosheets.[43] Because W does not alloy with Pd under the present reaction conditions, we propose that the relatively low redox potential of the W-decomposed form $W(CO)_6$ could help reduce the organopalladium(I) complex to Pd atoms rapidly in the early stage of the nucleation. The resultant W cations may simultaneously coordinate with Cl^- in the solution to form WCl_n complex. With the presence of ethanol, tungsten alkoxide intermediate could be produced and then converted to $W_{18}O_{49}$ with oxygen at elevated temperature[43,44]:

$$Pd^+ + W^0 \rightarrow W^{n+} + Pd^0 \tag{3}$$

$$W^{n+} + O_2 \rightarrow W_{18}O_{49} \tag{4}$$

$$WCl_n + \text{ethanol} \rightarrow \text{tungsten alkoxide} \tag{5}$$

$$\text{tungsten alkoxide} + O_2 \rightarrow W_{18}O_{49} \tag{6}$$

Overall, $W(CO)_6$ plays at least three roles in our synthesis: (1) To form coordination complexes with Pd(II) and thus speed the reduction rate; (2) to control the shape of Pd nanoparticles (tetrahedron vs irregular shapes); (3) to produce $W_{18}O_{49}$

Scheme 1. Mechanism Illustration for the Syntheses of (A) Pd Nanoparticles with Irregular Shapes by Using CO Molecules and (B) the Strongly Coupled Pd/W$_{18}$O$_{49}$ Hybrid Nanomaterials by Using W(CO)$_6$ Precursor
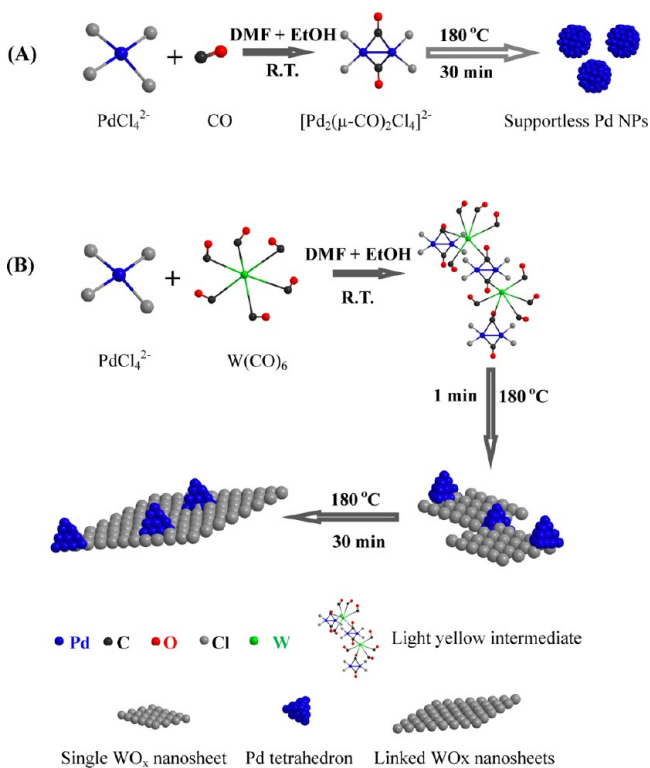
nanosheet supports for the nucleic, growth, and attachment of Pd nanotetrahedrons.

In addition to K$_2$PdCl$_4$ and W(CO)$_6$ precursors, PVP and CTAB are essential for the formation of Pd/W$_{18}$O$_{49}$ hybrids. Only aggregations of W$_{18}$O$_{49}$ nanosheets were obtained in the absence of PVP (Figure S12, Supporting Information). In addition, reaction in the presence of PVP but in the absence of CTAB yielded aggregated Pd nanoparticles with irregular shapes (Figure S13, Supporting Information). On the other hand, when the reaction was conducted in the absence of both PVP and CTAB, aggregates of both Pd and W$_{18}$O$_{49}$ were produced (Figure S14, Supporting Information). These results suggest that PVP and CTAB play important roles in the preferential growth of uniform tetrahedral Pd nanocrsytals and well-dispersed W$_{18}$O$_{49}$ nanosheets.

We also found that reaction temperature is another important factor for the morphology-controlled synthesis of Pd/W$_{18}$O$_{49}$ hybrids. Figure S15, Supporting Information, displays the representative TEM images of Pd/W$_{18}$O$_{49}$ obtained at different reaction temperatures. When reaction temperature is lower than 130 °C (Figure S15A,B), Pd tetrahedrons ($d \approx 16.45$ nm) supported on separated W$_{18}$O$_{49}$ nanosheets were formed. With reaction temperature elevated to 160 °C, larger Pd nanotetrahedrons ($d \approx 19.05$ nm) were formed and the single W$_{18}$O$_{49}$ nanosheets began to interconnect (Figure S15C). At a reaction temperature of 180 °C, well-dispersed and high-quality Pd nanotetrahedrons ($d \approx 19.67$ nm) supported on W$_{18}$O$_{49}$ nanosheets can be produced, as shown in Figure 5. However, with a further increase in reaction temperature to 200 °C, aggregates of Pd tetrahedrons ($d > 29$ nm) were obtained (Figure S15D). Therefore, 180 °C

is the optimal reaction temperature for the synthesis of Pd/W$_{18}$O$_{49}$ hybrid materials.

Based on the above results and discussion, a reasonable formation mechanism of Pd/W$_{18}$O$_{49}$ hybrid nanomaterials is proposed, as shown in Scheme 1B. First, reactive intermediate [Pd$_2$(μ-CO)$_2$Cl$_4$]$^{2-}$ was formed via the strong interaction between Pd^{2+} and W(CO)$_6$. Second, hydrothermal treatment induced the formation of tetrahedral Pd nanocrystals and a single W$_{18}$O$_{49}$ nanosheet. The strong covalent interaction between W and CO in W(CO)$_6$ could result in the simultaneous nucleation and growth of Pd nanotetrahedrons on the surface of W$_{18}$O$_{49}$ nanosheets. Here CO could serve as a bridge, which links Pd and W$_{18}$O$_{49}$. In addition, previous theoretical and experimental studies have found that oxygen vacancies in metal oxides, such as TiO$_2$ and MgO, are indeed the strongest metal binding sites.[53,54] As can been seen from the UV−vis spectrum of W$_{18}$O$_{49}$ nanosheets (Figure 4A), the considerably large absorption tail present in the visible and NIR regions clearly indicates the presence of a large number of oxygen vacancies on the surface of the W$_{18}$O$_{49}$ nanosheets,[44] which could serve as active sites for the nucleation and growth of Pd nanocrystals. This was confirmed by the disappearance of the large absorption tail after the formation of Pd/W$_{18}$O$_{49}$ hybrids. Finally, with reaction time increasing, Pd tetrahedrons with optimized size and exposed surface facets were produced while the single W$_{18}$O$_{49}$ nanosheet interconnected to form a 2D net structure.

Electrocatalytic Performance of Pd/W$_{18}$O$_{49}$ for the Oxygen Reduction Reaction (ORR). The intrinsic conductivity of the Pd/W$_{18}$O$_{49}$ was first evaluated by using the Fe(CN)$_6$$^{3-}$/Fe(CN)$_6$$^{4-}$ electrochemical probe. As shown in Figure S16, Supporting Information, the potential differences between the anodic and cathodic current peaks obtained from the Pd/W$_{18}$O$_{49}$, Pd NPs, Pd/C, Pt/C, and W$_{18}$O$_{49}$ nanosheets were measured to be 0.18, 0.15, 0.14, 0.14, and 0.35 V, respectively. It can be seen that although W$_{18}$O$_{49}$ nanosheets themselves exhibited low conductivity, the Pd/W$_{18}$O$_{49}$ hybrid nanomaterials demonstrated excellent electrical conductivity (similar to the Pd NPs, Pd/C, and Pt/C). To evaluate the electrocatalytic performance of the strongly coupled Pd/W$_{18}$O$_{49}$ hybrids for ORR, the polarization curve obtained from the Pd/W$_{18}$O$_{49}$ electrocatalyst thin film deposited on a rotating disk electrode (RDE) in an O$_2$-saturated 0.1 M KOH solution is shown in Figure 6A. For comparison, the polarization curves of ORR obtained from the commercial Pt/C, Pd/C, and the supportless Pd nanoparticles (Pd NPs) prepared in the absence of W(CO)$_6$ are also shown in Figure 6A (due to the low ORR activity of W$_{18}$O$_{49}$ nanosheets, the results are not shown here). In the electrochemical measurements, all the electrodes were pretreated by cycling the potential between 0.2 and 1.1 V (vs RHE) at a sweep rate of 100 mV/s for 50 cycles to remove surface contamination before the ORR activity tests. We can see that both Pd/W$_{18}$O$_{49}$ and Pd NPs have ORR onset potentials similar to that of Pt/C, which are nearly 60 mV higher than that of Pd/C. At higher overpotentials, the current reaches its diffusion-limited value, $\sim$$-5.8$ mA/cm^2 (geometric), which is within the 2% margin of the theoretical diffusion limiting current (i.e., -5.7 mA/cm^2),[55,56] clearly indicating a negligible contribution from O$_2$ diffusion through the Nafion film. At lower overpotentials (0.75 to 1.00 V), the currents are under the mixed kinetic/diffusion control, where mass transport plays an important role. In this mixed region, the ORR activity of the different catalysts can be
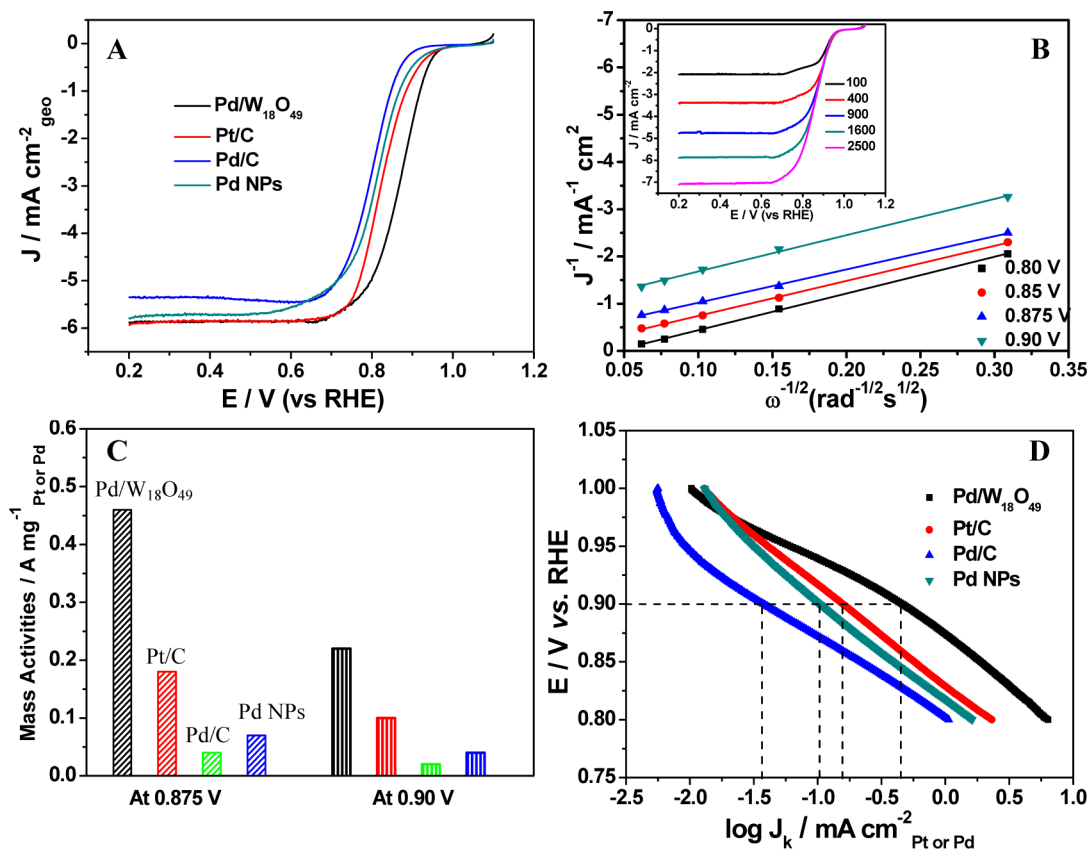
Figure 6. (A) ORR polarization curves on the strongly coupled $Pd/W_{18}O_{49}$ hybrids, Pt/C, Pd/C, and the supportless Pd nanoparticles in O_2-saturated 0.1 M KOH solution at room temperature, with rotation rate of 1600 rpm and a potential sweep rate of 10 mV/s. (B) Koutecky−Levich plots on $Pd/W_{18}O_{49}$ at different potentials. Symbols are experimental data from the corresponding rotating-disk voltammograms shown in the inset. Lines are the linear regressions. (C) Mass activities for $Pd/W_{18}O_{49}$, Pt/C, Pd/C, and the supportless Pd nanoparticles at 0.875 and 0.90 V. (D) Tafel plots from the different electrocatalysts and the comparison of their specific activities.

compared by evaluating the half-wave potentials, $E_{1/2}$ (that is, the potential at which the current reaches half its diffusion-limited value).

The ORR activities obtained from the commercial Pt/C and Pd/C in this work agree well with the previously reported data in the literature.[3,57] As clearly shown in Figure 6A, $E_{1/2}$ increases in the order of Pd/C < Pd NPs < Pt/C < Pd/$W_{18}O_{49}$. That is, the $Pd/W_{18}O_{49}$ hybrids show a remarkable positive shift in $E_{1/2}$ of ∼40, ∼70, and ∼80 mV relative to the Pt/C, Pd NPs, and Pd/C catalysts. Such results show that the strongly coupled $Pd/W_{18}O_{49}$ exhibits enhanced ORR electrocatalytic activity compared to the commercial Pt/C, Pd/C catalysts, and Pd NPs. The kinetic current (I_k) can be calculated from the Koutecky−Levich equation (details in Experimental Section). Figure 6B inset shows the rotating-disk voltammograms of the $Pd/W_{18}O_{49}$ hybrid (the corresponding voltammetric curves from the Pt/C, Pd/C, and Pd NPs are given in Figures S17−19, Supporting Information). The linearity of the Koutecky−Levich plots and the near parallelism of the fitting lines shown in Figure 6B suggest first-order reaction kinetics toward the concentration of dissolved oxygen and similar electron transfer numbers for ORR at different potentials.[58] On the basis of the slopes of the Koutecky−Levich plots, the electron transfer number (n) was calculated to be ∼4 at 0.75−0.9 V, indicating the nearly complete reduction of O_2 to H_2O on the surface of the $Pd/W_{18}O_{49}$ hybrid nanomaterials. To better understand the catalytic activities of electrocatalysts for the ORR, the mass activities (based on mass of Pd or Pt) and

the specific activities (based on electrochemically active surface area (ECSA)) at 0.875 and 0.90 V were calculated from the ORR polarization curves. As shown in Figure 6C, the Pd/$W_{18}O_{49}$ exhibits mass activity much higher than that of the other studied catalysts. Note that the intrinsic kinetic-current density at 0.90 V is usually used as a standard metric for the comparison of activities of different ORR catalysts. The mass activity of the $Pd/W_{18}O_{49}$ at 0.90 V was calculated to be 0.216 A/mg, which is nearly 2, 6, and 10 times higher than those of the commercial Pt/C (0.1 A/mg), Pd NPs (0.038 A/mg), and Pd/C (0.02 A/mg), respectively. Figure 6D compares the specific activities (I_k) of $Pd/W_{18}O_{49}$, Pt/C, Pd/C, and Pd NPs toward the ORR. I_k was obtained from mass-transport-corrected Tafel plots by normalizing the kinetic current to the ECSA. Here the ECSA was calculated by measuring the charge associated with the hydrogen adsorption/desorption region after double-layer correction from the cyclic voltammograms (Figure S20, Supporting Information) and assuming a value to 0.21 mC/cm^2 for the adsorption of a hydrogen monolayer on Pt surface for Pt-based catalysts, while the ECSA of Pd was obtained by assuming that the monolayer PdO reduction charge is 0.405 mC/cm^2 on the Pd surface for Pd-based catalysts.[23,25] The ECSA of the strongly coupled Pd/$W_{18}O_{49}$ hybrids was determined to be ≈48.0 m^2/g_{Pd}, comparable to that of the commercial Pd/C of ≈40 m^2/g. From Figure 6D, the specific activity of the $Pd/W_{18}O_{49}$ at 0.90 V was measured to be 0.45 mA/cm^2_{Pd}, which is much higher than those of commercial Pt/C (0.16 mA/cm^2_{Pt}), Pd/C (0.02

mA/cm$^2_{Pd}$), and Pd NPs (0.04 mA/cm$^2_{Pd}$). The Tafel plots of all the electrodes have two linear regions with slopes of −120 mV/dec at high overpotential range and around −60 mV/dec at low overpotential range. At potentials below 0.92 V, the slopes of the curves are approximately equal, suggesting almost the same reaction mechanism of ORR on the different electrodes over the majority of the potential range. While there is a slight difference in slope at low overpotential range that may be associated with different mechanisms on the electrocatalysts in this potential region.[59] The ORR results from the four electrocatalysts are summarized in Table 1. Note that

Table 1. Electrocatalytic Performance of Pd/W$_{18}$O$_{49}$, Pt/C, Pd/C, and Supportless Pd Nanoparticles (Pd NPs) for ORR

sample	ECSA (m^2/g)	$E_{1/2}$ (V)	mass activities (at 0.9 V, A/mg)	I_k (at 0.9 V, mA/cm$^2_{Pt\ or\ Pd}$)
Pd/ W$_{18}$O$_{49}$	48.0	0.875	0.216	0.45
Pt/C	59.8	0.835	0.10	0.16
Pd/C	40	0.79	0.02	0.038
Pd NPs	38.6	0.805	0.038	0.10

all the polarization curves in our measurements were recorded from the cathodic (or negative) sweep, that is, from 1.1 to 0.2 V. Earlier studies have shown that the anodic (or positive) sweep may induce a positive-shifted $E_{1/2}$.[6,57,60,61] Here the anodic linear sweep voltammograms were also measured on the Pd/W$_{18}$O$_{49}$ and Pt/C (Figure S21, Supporting Information), from which positively shifted $E_{1/2}$ was indeed observed. Surprisingly, the onset and $E_{1/2}$ potentials of ORR on the strongly coupled Pd/W$_{18}$O$_{49}$ hybrids are ca. 1.08 and 0.932 V vs RHE, respectively, while the onset and $E_{1/2}$ potentials on the commercial Pt/C catalyst are 1.04 and 0.863 V, respectively. As far as we know, the highest ORR onset and $E_{1/2}$ potentials to date were obtained in acid electrolytes with single-crystalline Pt$_3$Ni catalyst (ORR onset potential ca. 1.0 V, $E_{1/2}$ ca. 0.92 V)[10] and nanoporous PtNi catalyst (ORR onset potential ca. 1.05 V, $E_{1/2}$ ca. 0.96 V).[59] Thus, the electrocatalytic performance of the Pd/W$_{18}$O$_{49}$ hybrid catalysts developed in this work not only significantly exceeds that of any previously reported Pt-based catalyst in alkaline media but also is at least comparable to that of the most Pt-alloy catalysts in acidic media.

To further examine the stability of the electrocatalysts, the accelerated durability tests (ADTs) of the catalysts were conducted by potential cycling between 0.6 and 1.0 V vs RHE in O$_2$-saturated 0.1 M KOH solution. It can be seen from Figure 7A that after 10,000 potential cycles, the supportless Pd nanoparticles showed a degradation of more than 160 mV in its half-wave potential, $E_{1/2}$. Simultaneously, the diffusion-limiting currents decreased significantly, which indicates the loss of Pd nanoparticles from the electrode surface. However, the strongly coupled Pd/W$_{18}$O$_{49}$ catalyst exhibited only 24 mV degradation in the half-wave potential without noticeable decrease of the diffusion-limiting currents, indicating the enhanced durability of Pd nanocrystals supported on W$_{18}$O$_{49}$ nanosheets. The TEM image of the Pd/W$_{18}$O$_{49}$ catalyst after ADTs measurements (Figure 7B) indicates that most of the Pd nanocrystals are still well-dispersed on the W$_{18}$O$_{49}$ nanosheets without significant aggregation and shape change, which further demonstrates the high stability of the W$_{18}$O$_{49}$ nanosheet-supported Pd nano-particles. The high durability of Pd/W$_{18}$O$_{49}$ could be ascribed to the ultrahigh chemical stability of W$_{18}$O$_{49}$ and the strong interaction between Pd and W$_{18}$O$_{49}$. For comparison, the
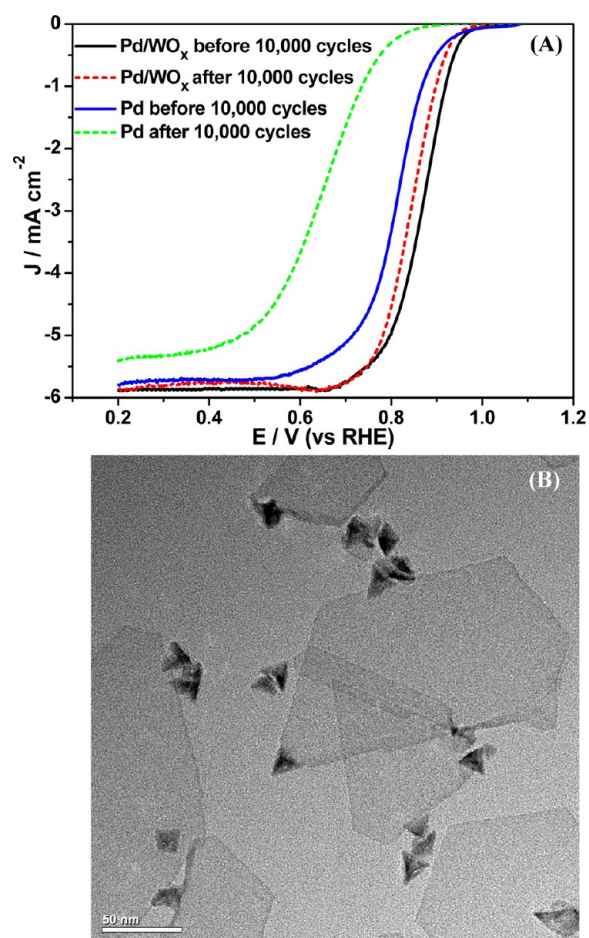

Figure 7. (A) Polarization curves for the ORR on the Pd/W$_{18}$O$_{49}$ and supportless Pd nanoparticles before and after 10 000 potential cycles in O$_2$-saturated 0.1 M KOH solution at room temperature with a potential sweep rate of 10 mV/s and a rotation rate of 1600 rpm. (B) TEM image of the Pd/W$_{18}$O$_{49}$ hybrid nanomaterials after 10 000 potential cycles.

ADTs of the commercial Pt/C and Pd/C catalysts were also evaluated. As can be seen from Figure S22, the commercial catalysts showed significant decrease of the diffusion-limiting currents and degradation of almost 60 and 100 mV in their half-wave potentials, respectively.

Both activity and durability studies indicate that the W$_{18}$O$_{49}$ nanosheets could serve as an efficient catalyst support materials to promote the catalytic activity and stability of Pd nanocrystals toward ORR. Generally, O$_2$ activation involves a proton and electron transfer to form adsorbed OOH before the O−O bond is broken.[31] Therefore, to achieve high ORR catalytic activity, a catalyst should be able to stabilize OOH moderately. After dissociation, adsorbed O and OH are formed on the catalyst surface, and to make a fast H$_2$O desorption, the catalyst should not bind these species too strongly. Thus, to design a better catalyst than Pt for ORR, the catalyst should counterbalance two opposing effects, that is, a relatively strong adsorption energy of O$_2$ and reaction intermediates (O$_2^-$, O$_2^{2-}$, H$_2$O$_2$, and so on) and a relatively low coverage by spectator oxygenated species and specifically adsorbed anions.[29,62] Recently, both theoretical calculations and experimental results have shown that oxygen binds more strongly on Pd than on Pt.[27,63] Due to the high adsorption strength of O$_2$ on Pd, the O−O bonds can be broken easily, but this generates a high coverage by
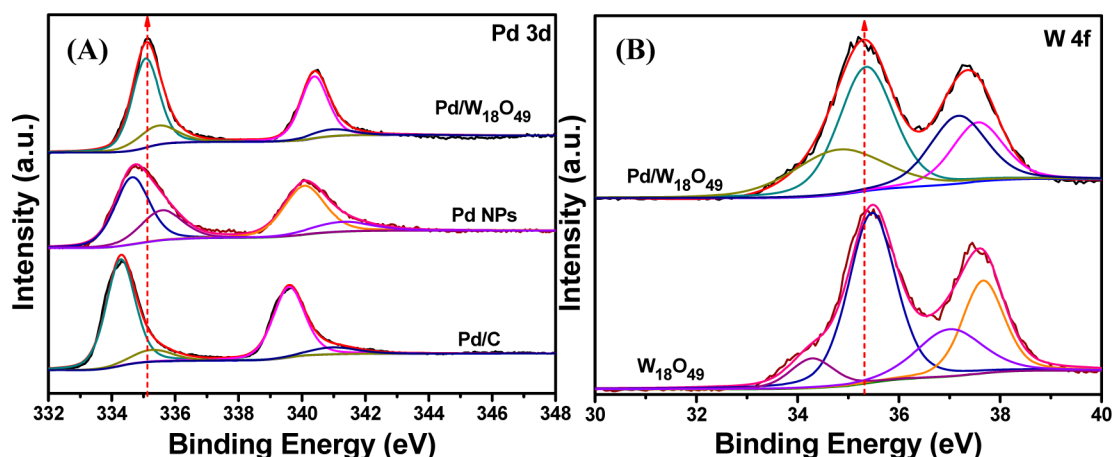
Figure 8. (A) XPS patterns of Pd 3d in Pd/$W_{18}O_{49}$, Pd NPs, and commercial Pd/C. (B) XPS pattern of W 4f in Pd/$W_{18}O_{49}$ and $W_{18}O_{49}$.

oxygenated intermediates that are slowly desorbed.[10] Thus, a decrease in electron density in Pd, which may weaken the Pd—O bond, could substantially enhance the dissociative adsorption of O_2.[64,26,63] Furthermore, previous studies also found that a decrease in electron density could decrease the superficial coverage by OH_{ad} from water activation, leading to an increase in the number of free active sites for O_2 adsorption.[65] In the case of the present strongly coupled Pd/$W_{18}O_{49}$ hybrids, the strong interaction between Pd nanocrystals and $W_{18}O_{49}$ support can significantly improve the electrocatalytic performance. Figure 8 shows that the incorporation of $W_{18}O_{49}$ did markedly alter the electronic structure of Pd. For instance, the binding energy of Pd 3d has a positive-shift compared to the supportless one. This positive shift could therefore decrease the electron density (downshift of the d-band center) in Pd and then weaken the Pd—O bond strength, making the Pd surface easily accessible for O_2 adsorption and activation.[26,63,64,17] On the other hand, the binding energy of W 4f for Pd/$W_{18}O_{49}$ was negative-shifted compared to that of pure $W_{18}O_{49}$ (Figure 8B) and the early reported materials, which further indicates the strong interaction between Pd and $W_{18}O_{49}$ in the as-synthesized Pd/$W_{18}O_{49}$ hybrid nanomaterials. In addition, due to the presence of excess oxygen vacancies, the electronic conductivity of $W_{18}O_{49}$ could be significantly increased. Overall, the large surface area and high chemical stability of $W_{18}O_{49}$ nanosheets and the strong interaction between Pd and $W_{18}O_{49}$ account for the enhanced ORR activity and stability of the Pd/$W_{18}O_{49}$ hybrids.

4. CONCLUSIONS

In summary, we have developed a robust method for the synthesis of strongly coupled Pd/$W_{18}O_{49}$ hybrid nanomaterials that demonstrated very high activity and durability for ORR compared with commercial Pt/C and Pd/C catalysts in alkaline media. The unique $[Pd_2(\mu\text{-CO})_2Cl_4]^{2-}$-$W(CO)_6$ structure provides a powerful means to tailor the morphology of Pd nanocrystals and to synthesize metal oxide nanosheet-suppoprted nanocatalysts. We found that although supportless Pd nanoparticles or $W_{18}O_{49}$ alone has low catalytic activity toward ORR, their hybrids exhibited not only surprisingly high ORR activity but also superior stability to Pt in alkaline solutions. These results suggest that the activity enhancement is a result of electronic structure change of Pd upon its synergistic interaction with the $W_{18}O_{49}$ nanosheet support. We believe that the strategy presented in this study could afford strong chemical

attachment and electrical coupling between the nanoelectrocatalysts and support materials and is expected to open up exciting opportunities for developing a novel class of hybrid nanomaterials with improved activity and durability for the ORR in fuel cells and metal—air batteries.

■ ASSOCIATED CONTENT

ⓢ Supporting Information

Additional structure characterizations and more electrochemical measurements of the as-prepared materials. This material is available free of charge via the Internet at http://pubs.acs.org.

■ AUTHOR INFORMATION

Corresponding Author
weichen@ciac.ac.cn

Notes
The authors declare no competing financial interest.

■ ACKNOWLEDGMENTS

■ REFERENCES

(1) Winter, M.; Brodd, R. J. *Chem. Rev.* **2004**, *104*, 4245−4269.
(2) Liu, M. M.; Zhang, R. Z.; Chen, W. *Chem. Rev.* **2014**, *114*, 5117−5160.
(3) Shao, M. *J. Power Sources* **2011**, *196*, 2433−2444.
(4) Black, R.; Adams, B.; Nazar, L. F. *Adv. Energy Mater.* **2012**, *2*, 801−815.
(5) Cao, R.; Lee, J. S.; Liu, M. L.; Cho, J. *Adv. Energy Mater.* **2012**, *2*, 816−829.
(6) Strasser, P.; Koh, S.; Anniyev, T.; Greeley, J.; More, K.; Yu, C. F.; Liu, Z. C.; Kaya, S.; Nordlund, D.; Ogasawara, H.; Toney, M. F.; Nilsson, A. *Nat. Chem.* **2010**, *2*, 454−460.
(7) van der Vliet, D. F.; Wang, C.; Tripkovic, D.; Strmcnik, D.; Zhang, X. F.; Debe, M. K.; Atanasoski, R. T.; Markovic, N. M.; Stamenkovic, V. R. *Nat. Mater.* **2012**, *11*, 1051−1058.
(8) Chen, A. C.; Holt-Hindle, P. *Chem. Rev.* **2010**, *110*, 3767−3804.
(9) Chen, W.; Kim, J. M.; Sun, S. H.; Chen, S. W. *J. Phys. Chem. C* **2008**, *112*, 3891−3898.
(10) Stamenkovic, V. R.; Fowler, B.; Mun, B. S.; Wang, G. F.; Ross, P. N.; Lucas, C. A.; Markovic, N. M. *Science* **2007**, *315*, 493−497.
(11) Liu, M. M.; Chen, W. *Nanoscale* **2013**, *5*, 12558−12564.
(12) Jiang, Y. Y.; Lu, Y. Z.; Lv, X. Y.; Han, D. X.; Zhang, Q. X.; Niu, L.; Chen, W. *ACS Catal.* **2013**, *3*, 1263−1271.

(13) Zhang, R. Z.; Chen, W. *J. Mater. Chem. A* **2013**, *1*, 11457−11464.

(14) Wu, H. B.; Chen, W. *J. Am. Chem. Soc.* **2011**, *133*, 15236−15239.

(15) Chen, W.; Chen, S. W. *Angew. Chem., Int. Ed.* **2009**, *48*, 4386−4389.

(16) Lu, Y. Z.; Wang, Y. C.; Chen, W. *J. Power Sources* **2011**, *196*, 3033−3038.

(17) Shao, M. H.; Huang, T.; Liu, P.; Zhang, J.; Sasaki, K.; Vukmirovic, M. B.; Adzic, R. R. *Langmuir* **2006**, *22*, 10409−10415.

(18) Suo, Y. G.; Zhuang, L.; Lu, J. T. *Angew. Chem., Int. Ed.* **2007**, *46*, 2862−2864.

(19) Xiao, L.; Zhuang, L.; Liu, Y.; Lu, J. T.; Abruna, H. D. *J. Am. Chem. Soc.* **2009**, *131*, 602−608.

(20) Wei, W. T.; Chen, W. *J. Power Sources* **2012**, *204*, 85−88.

(21) Jiang, L.; Hsu, A.; Chu, D.; Chen, R. *J. Electrochem. Soc.* **2009**, *156*, B370−B376.

(22) Li, B.; Prakash, J. *Electrochem. Commun.* **2009**, *11*, 1162−1165.

(23) Seo, M. H.; Choi, S. M.; Kim, H. J.; Kim, W. B. *Electrochem. Commun.* **2011**, *13*, 182−185.

(24) Jiang, L.; Hsu, A.; Chu, D.; Chen, R. *J. Electrochem. Soc.* **2009**, *156*, B643−B649.

(25) Poon, K. C.; Tan, D. C.; Vo, T. D.; Khezri, B.; Su, H.; Webster, R. D.; Sato, H. *J. Am. Chem. Soc.* **2014**, *136*, 5217−5220.

(26) Zhang, Z. H.; Wang, X. G.; Cui, Z. M.; Liu, C. P.; Lu, T. H.; Xing, W. *J. Power Sources* **2008**, *185*, 941−945.

(27) Lima, F. H. B.; Zhang, J.; Shao, M. H.; Sasaki, K.; Vukmirovic, M. B.; Ticianelli, E. A.; Adzic, R. R. *J. Phys. Chem. C* **2007**, *111*, 404−410.

(28) Zhang, J. L.; Vukmirovic, M. B.; Xu, Y.; Mavrikakis, M.; Adzic, R. R. *Angew. Chem., Int. Ed.* **2005**, *44*, 2132−2135.

(29) Stamenkovic, V. R.; Mun, B. S.; Arenz, M.; Mayrhofer, K. J. J.; Lucas, C. A.; Wang, G. F.; Ross, P. N.; Markovic, N. M. *Nat. Mater.* **2007**, *6*, 241−247.

(30) Stamenkovic, V.; Mun, B. S.; Mayrhofer, K. J. J.; Ross, P. N.; Markovic, N. M.; Rossmeisl, J.; Greeley, J.; Norskov, J. K. *Angew. Chem., Int. Ed.* **2006**, *45*, 2897−2901.

(31) Norskov, J. K.; Rossmeisl, J.; Logadottir, A.; Lindqvist, L.; Kitchin, J. R.; Bligaard, T.; Jonsson, H. *J. Phys. Chem. B* **2004**, *108*, 17886−17892.

(32) Van, T. T. H.; Pan, C. J.; Rick, J.; Su, W. N.; Hwang, B. J. *J. Am. Chem. Soc.* **2011**, *133*, 11716−11724.

(33) Toyoda, E.; Jinnouchi, R.; Ohsuna, T.; Hatanaka, T.; Aizawa, T.; Otani, S.; Kido, Y.; Morimoto, Y. *Angew. Chem., Int. Ed.* **2013**, *52*, 4137−4140.

(34) Huang, S. Y.; Ganesan, P.; Park, S.; Popov, B. N. *J. Am. Chem. Soc.* **2009**, *131*, 13898−13899.

(35) Awaludin, Z.; Suzuki, M.; Masud, J.; Okajima, T.; Ohsaka, T. *J. Phys. Chem. C* **2011**, *115*, 25557−25567.

(36) Liu, Y.; Shrestha, S.; Mustain, W. E. *ACS Catal.* **2012**, *2*, 456−463.

(37) Lu, Y. Z.; Jiang, Y. Y.; Chen, W. *Nanoscale* **2014**, *6*, 3309−3315.

(38) Li, H.; Chen, G. X.; Yang, H. Y.; Wang, X. L.; Liang, J. H.; Liu, P. X.; Chen, M.; Zheng, N. F. *Angew. Chem., Int. Ed.* **2013**, *52*, 8368−8372.

(39) Huang, X. Q.; Tang, S. H.; Mu, X. L.; Dai, Y.; Chen, G. X.; Zhou, Z. Y.; Ruan, F. X.; Yang, Z. L.; Zheng, N. F. *Nat. Nanotechnol.* **2011**, *6*, 28−32.

(40) Polleux, J.; Pinna, N.; Antonietti, M.; Niederberger, M. *J. Am. Chem. Soc.* **2005**, *127*, 15595−15601.

(41) Gracia-Espino, E.; Hu, G. Z.; Shchukarev, A.; Wagberg, T. *J. Am. Chem. Soc.* **2014**, *136*, 6626−6633.

(42) Wang, X. X.; Yang, J. D.; Yin, H. J.; Song, R.; Tang, Z. Y. *Adv. Mater.* **2013**, *25*, 2728−2732.

(43) Moshofsky, B.; Mokari, T. *Chem. Mater.* **2013**, *25*, 1384−1391.

(44) Xi, G. C.; Ouyang, S. X.; Li, P.; Ye, J. H.; Ma, Q.; Su, N.; Bai, H.; Wang, C. *Angew. Chem., Int. Ed.* **2012**, *51*, 2395−2399.

(45) Zhang, H. Y.; Huang, C. L.; Tao, R. T.; Zhao, Y. F.; Chen, S.; Sun, Z. Y.; Liu, Z. M. *J. Mater. Chem.* **2012**, *22*, 3354−3359.

(46) Sahoo, P. K.; Kamal, S. S. K.; Premkumar, M.; Sreedhar, B.; Srivastava, S. K.; Durai, L. *Int. J. Refract. Met. Hard Mater.* **2011**, *29*, 547−554.

(47) Sahoo, P. K.; Kamal, S. S. K.; Premkumar, M.; Kumar, T. J.; Sreedhar, B.; Singh, A. K.; Srivastava, S. K.; Sekhar, K. C. *Int. J. Refract. Met. Hard Mater.* **2009**, *27*, 784−791.

(48) Xiong, L. F.; He, T. *Chem. Mater.* **2006**, *18*, 2211−2218.

(49) Lee, K.; Seo, W. S.; Park, J. T. *J. Am. Chem. Soc.* **2003**, *125*, 3408−3409.

(50) Paracchini, C.; Schianchi, G. *Phys. Status Solidi A* **1982**, *72*, K129−K132.

(51) Manfredi, M.; Paracchini, C.; Salviati, G. C.; Schianchi, G. *Thin Solid Films* **1981**, *79*, 161−166.

(52) Sahoo, P. K.; Kamal, S. S. K.; Durai, L.; Sreedhar, B. *J. Mater. Res.* **2011**, *26*, 652−657.

(53) Wahlstrom, E.; Lopez, N.; Schaub, R.; Thostrup, P.; Ronnau, A.; Africh, C.; Laegsgaard, E.; Norskov, J. K.; Besenbacher, F. *Phys. Rev. Lett.* **2003**, *90*, 026101.

(54) Giordano, L.; Goniakowski, J.; Pacchioni, G. *Phys. Rev. B* **2001**, *64*, 075417.

(55) Mayrhofer, K. J. J.; Strmcnik, D.; Blizanac, B. B.; Stamenkovic, V.; Arenz, M.; Markovic, N. M. *Electrochim. Acta* **2008**, *53*, 3181−3188.

(56) Garsany, Y.; Baturina, O. A.; Swider-Lyons, K. E.; Kocha, S. S. *Anal. Chem.* **2010**, *82*, 6321−6328.

(57) Wang, D. L.; Xin, H. L. L.; Hovden, R.; Wang, H. S.; Yu, Y. C.; Muller, D. A.; DiSalvo, F. J.; Abruna, H. D. *Nat. Mater.* **2013**, *12*, 81−87.

(58) Liang, Y. Y.; Li, Y. G.; Wang, H. L.; Zhou, J. G.; Wang, J.; Regier, T.; Dai, H. *J. Nat. Mater.* **2011**, *10*, 780−786.

(59) Snyder, J.; Fujita, T.; Chen, M. W.; Erlebacher, J. *Nat. Mater.* **2010**, *9*, 904−907.

(60) Gasteiger, H. A.; Kocha, S. S.; Sompalli, B.; Wagner, F. T. *Appl. Catal., B* **2005**, *56*, 9−35.

(61) Chung, H. T.; Won, J. H.; Zelenay, P. *Nat. Commun.* **2013**, *4*, 1922.

(62) Greeley, J.; Stephens, I. E. L.; Bondarenko, A. S.; Johansson, T. P.; Hansen, H. A.; Jaramillo, T. F.; Rossmeisl, J.; Chorkendorff, I.; Norskov, J. K. *Nat. Chem.* **2009**, *1*, 552−556.

(63) Seo, M. H.; Choi, S. M.; Seo, J. K.; Noh, S. H.; Kim, W. B.; Han, B. *Appl. Catal., B* **2013**, *129*, 163−171.

(64) Sarkar, A.; Murugan, A. V.; Manthiram, A. *J. Mater. Chem.* **2009**, *19*, 159−165.

(65) Mukerjee, S.; Srinivasan, S.; Soriaga, M. P.; Mcbreen, J. *J. Electrochem. Soc.* **1995**, *142*, 1409−1422.